



# Hierarchical porous metallic glass with strong broadband absorption and photothermal conversion performance for solar steam generation

Jianan Fu<sup>a</sup>, Zhen Li<sup>b</sup>, Xin Li<sup>a</sup>, Fei Sun<sup>a</sup>, Luyao Li<sup>a</sup>, Hongzhen Li<sup>c</sup>, Jinlai Zhao<sup>d</sup>, Jiang Ma<sup>a,\*</sup>

<sup>a</sup> Shenzhen Key Laboratory of High Performance Nontraditional Manufacturing, College of Mechatronics and Control Engineering, Shenzhen University, Shenzhen 518060, China

<sup>b</sup> Department of Mechanics and Aerospace Engineering, Southern University of Science and Technology, Shenzhen 518055, Guangdong, China

<sup>c</sup> National Engineering Research Center of Near-net-shape Forming for Metallic Materials, South China University of Technology, Guangzhou 510640, China

<sup>d</sup> College of Materials Science and Engineering, Shenzhen Key Laboratory of Polymer Science and Technology, Guangdong Research Center for Interfacial Engineering of Functional Materials, Shenzhen 518060, China

## ARTICLE INFO

### Keywords:

Metallic glass  
Hierarchical porous structure  
Strong absorption  
Photothermal conversion  
Solar steam generation

## ABSTRACT

The development of a strong light absorption absorber with a facile preparation process are crucial for some photothermal conversion applications, such as solar steam generation, photothermal catalysis and detectors. Here, a hierarchical structure based on microporous surface equipped with nanoporous layer is ingeniously designed and fabricated benefiting from the unique thermoplastic forming ability of metallic glasses by using the soluble clusters as template in less than 30 s. The presence of hierarchical porous structures induces multiple reflection of light and excites the plasmonic behavior of surface, achieving over 90% light absorption in the 380–20 μm wavelength range and the broad light incident angle from 0° to 70°, resulting in a remarkable photothermal conversion performance. Compared to conventional and existing absorber, the innovatively designed and fabricated metallic surface offers outstanding advantages in terms of light absorption range, heating rate and maximum temperature rise. Afterwards, the hierarchical porous structures for solar steam generation shows an evaporation efficiency of up to 94.2% and evaporation rate of 1.72 kg m<sup>-2</sup> h<sup>-1</sup> at 1 kW m<sup>-2</sup>. The design of unprecedented structure on metallic glass opens up a new strategy for solar energy harvesting, water treatment and other related fields.

## 1. Introduction

With the concept of a green Earth continues to be promoted, renewable green energy has begun to receive tremendous attention. Solar energy as one of the world's ubiquitous green energy, due to it strikes into the earth every day is much greater than the energy consumed by the earth in a year [1,2], is widely used and researched in the fields of the solar power generation [3–5], seawater desalination [6–8], crude oil recovery [9–11], and sterilization [12,13] etc. Solar steam generations have recently begun to appear on the horizon and become a topic of growing interest research for scientists as they will greatly improve the global serious water shortage [14–17]. The core component of solar steam generation is an absorber with strong light absorption. Desirable solar steam generations require absorbers that not only efficiently photothermal conversion but also have excellent hydrophilicity, so that the seawater on its surface can drive water to form

steam under the solar irradiation, achieving the purpose of seawater desalination or sewage treatment [18]. So far, numerous technological solar steam generations with considerable evaporation efficiency have been reported such as nano fibrous aerogels [19], graphene foam [20], mxene-based hierarchical architecture [21]. However, the tedious preparation process and the insufficient stability are often overlooked which greatly limit their practical applications. To tackle the challenge, developing solar steam generations with convenient fabrication process and robust properties will have bright prospects.

Metallic glasses (MGs), i. e. amorphous alloys, have received extensively attention since they were discovered, due to the unique properties [22–31]. The absence of grain boundaries and crystal defects comparing with crystalline alloys endows MGs with superior corrosion resistance [32,33]. Meanwhile, the MGs can be thermoplastically formed like the plastics when heated to a certain temperature, so that the nanoscale structures can be facilely and precisely fabricated on the MGs to

\* Corresponding author.

E-mail address: [majiang@szu.edu.cn](mailto:majiang@szu.edu.cn) (J. Ma).

<https://doi.org/10.1016/j.nanoen.2022.108019>

Received 23 May 2022; Received in revised form 28 October 2022; Accepted 15 November 2022

Available online 21 November 2022

2211-2855/© 2022 Elsevier Ltd. All rights reserved.

generate a surface with strong absorption and photothermal conversion performance [34,35], which makes them a promising candidate material for solar steam generations.

Among various nano/micro structures, hierarchical porous (HP) structures are considered to be the optimal structure for solar steam generations, as the porous structures have large specific surface area to provide sufficient heat transfer, the porous channel can facilitate steam release [20,36]. Although the methods of dealloying [37] and pitting [38] can prepare the porous structures on the MGs, the intrinsic amorphous property of the MGs will be transformed during the fabrication process and the aspect ratio of the micro structures is limited, not appropriate for the strong absorption and photothermal conversion performance. Therefore, the fabrication of HP structures with its required performance for solar steam generation on the MGs is still perceived as an open question.

In this work, we design the hierarchical porous structures on the MG (HP-MG), fabricated by a novel method of using the soluble clusters as template in just 30 s. HP-MG exhibits the characteristics of microscale pores accompanied with mesopores and maintain intrinsic amorphous nature. Optically, the absorber of HP-MG achieves more than 90% light absorption in the 380–20  $\mu\text{m}$  wavelength range and the broad light incident angle ( $\theta_{inc}$ ) from  $0^\circ$  to  $70^\circ$ , and it shows better sensitive photothermal response than the MG plate under different laser with wavelengths of 405, 532, 655, 808, and 1064 nm. When the 808 nm laser power is increased to  $6 \text{ W/cm}^2$ , the HP-MG can heat up to  $\sim 130^\circ\text{C}$ , and the heating rate reaches an exciting  $32.35^\circ\text{C/s}$ . Based on the outstanding absorption performance, HP-MG exhibits a solar evaporation efficiency as high as 94.2% when used as a solar steam generation at  $1 \text{ kW m}^{-2}$ . HP-MG, furthermore, also shows remarkable purification characteristics in seawater desalination and sewage treatment. We believe that the novel strategy will inspire and create more meaningful hierarchical micro/nano structures, and it will make multifunctional usage of energy conversion.

## 2. Results and discussion

### 2.1. Fabrication and Characterization of HP-MG

The schematic illustration of fabricating HP-MG is shown in the Fig. 1a. MGs has excellent flowability in the supercooled liquid region (SLR) [23,28], so that the MGs will fill the gap between the nanopowders and wrap it under the pressure. When the powder is dissolved and removed by suitable chemical solvent after the thermoplastic forming (TPF), corresponding HP structure is fabricated on the surface of MGs. Fig. 1b meticulously depicts the formation of each level structure. The nanopowders tend to cluster into particles with different sizes, which plays a critical role in the fabrication of HP structures during the TPF [39]. The formation of large pores and small pores are controlled by clusters of large particles and small particles, respectively, while the formation of mesopores on the MG is caused by the nanopowder embedded in the clusters. Taking advantage of the multiscale clusters feature of nanopowders, HP structure is successfully fabricated on the MG (Fig. 1c, d, e), and the insets show the clusters used for forming the corresponding pore-scale structure and the nanopowders on the clusters. It can be observed that small pores are distributed on the large pores, and the inner walls of the large pores are densely covered with mesopores. The scanning electron microscopy (SEM) images of the HP-MG fracture morphology (Fig. S1) intuitively confirm the HP structures on the MG. It is worth noting that there is a mesoporous layer connected to the MG substrate around the large pore, which will induce the HP-MG to effectively absorb light of different wavelengths [40,41]. The HP-MG pore size distribution is quantitatively determined by the SEM image (Fig. 1f). Micro-scale pores and nano-scale mesopores are mostly found on HP-MG from the size distribution, and the size of the mesopores agrees with the original particle size of the nanopowder used. Typically, Fig. 1g shows the transmission electron microscopy (TEM) image of

HP-MG, which the diameter ( $\sim 40 \text{ nm}$ ) of single mesopore can be clearly observed on the MG substrate. The high-resolution TEM images in Fig. 1h demonstrate that atomic arrangement around a single mesopore is disorder, indicating that HP-MG are fully amorphous. The diffractive halo-like selected area electron diffraction pattern (insert in the Fig. 1h) and the X-ray diffraction (XRD) pattern of the HP-MG (Fig. S2) without crystallization peak verify this. Fig. 1i shows the images of TEM element mapping, and the Pt, Ni, Cu, P is homogeneously distributed on the cross-sectional mesoporous structure of HP-MG, proving that no elemental segregation occurs in HP-MG during the TPF.

### 2.2. The Optical Performance of HP-MG

The HP structure was fabricated on the MG resulting in several its surface functional property variations, among the intuitive changes are the optical performance. Fig. 2a shows the photographic image of HP-MG under the natural environment. It can be observed that the surface containing the HP structure exhibits very black feature, which strongly contrasts with the silvery color shown by the surrounding structureless edges. Then, the reflectance spectrum of HP-MG was quantitatively measured in the broadband range, and the reflectance spectrum of MG plate is also added in as a comparison (Fig. 2g, h, i). Remarkably, The HP-MG achieves extremely low reflectance ( $< 5\%$  at visible region and near infrared region,  $< 10\%$  at middle infrared region), which is superior to the MG plate. The results indicate that the HP structure design is capable of absorbing up to 90% of the light in broadband range. To further investigate the light absorption mechanism of the absorber with the HP structure, the FDTD combined with the optical constants of MG plate (Fig. 2b) was used for simulation modeling and analysis. After the model is constructed (see Experimental section), the simulated reflection spectrum is shown in Fig. 2c. From the simulated reflectance spectrum, this information can be found that: 1) the simulated reflectance spectrum also exhibits very low reflectance ( $< 5\%$ ) in the wavelength range of 380–2500 nm; 2) The trend of the simulated reflectance curve is gradually upward. The results mean the experimental reflectance of the HP-MG is reproduced well by the simulated reflectance spectrum from 380 nm to 2500 nm and the mechanism of the absorption for the HP-MG can be well obtained by model of the FDTD simulation. Meanwhile, we also simulated the dependence of  $\theta_{inc}$  on the absorption of the HP-MG. The left Fig. 2d shows the schematic illustration of different  $\theta_{inc}$  to HP-MG, and the average absorption obtained from the corresponding  $\theta_{inc}$  is summarized in right Fig. 2d (Fig. S3). In total, the HP-MG can achieve over 90% absorption in a broad  $\theta_{inc}$  from  $0^\circ$  to  $70^\circ$ .

The broadband and wide-angle light absorption properties can be attributed to the rough morphology of HP-MG and the metallic material used. First of all, due to the HP-MG is composed of micro/nano-scale porous structures, when light hits the HP-MG it will get trapped in the porous gap. In this condition, the light will be repeatedly reflected in the pores until complete absorption (Fig. 2e). Additionally, the four arbitrary calculated cross-sectional electric field distributions were selected in the Fig. 2f. It can be seen that the calculated cross-sectional electric field widely spread hot spots. This hot spots indicate that very strong localized surface plasmon resonance (LSPR) occur, leading to absorption enhancement [42]. Thus, the excellent absorption of the HP-MG in broadband and wide-angle region is attributed to the common effects of the light trapping and the excitations of high-density LSPR.

### 2.3. The Photothermal Conversion Performance of HP-MG

The HP-MG offers a great potential application in the field of photothermal conversion due to its strong absorption in broadband. Based on these advantages, the photothermal conversion performance of the HP-MG was evaluated by irradiation with lasers of different wavelengths. To compare different properties of the surface structures, the photothermal conversion performance of MG plate and HP-MG was measure under the same condition. Fig. 3a shows the schematic of

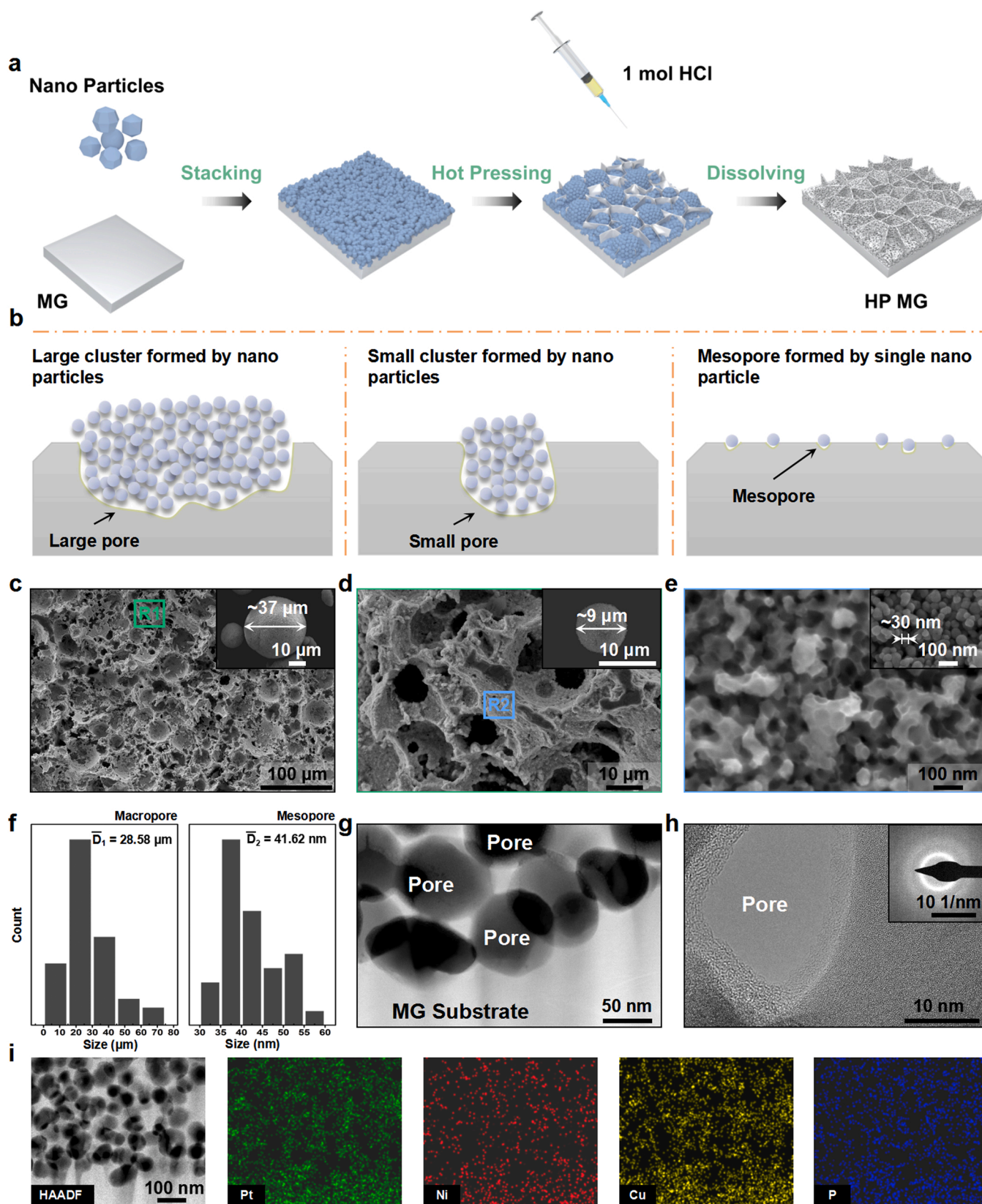


**Fig. 1.** The characterization of HP-MG. (a) The schematic illustration of fabricating the HP-MG. (b) The formation details of large pore, small pore and the mesopore in the HP-MG. (c) The SEM images of the large pore on the HP-MG, the inset shows the SEM image of single powder particle forming corresponding large pores. (d) The SEM image of the small pore on the HP-MG, the inset shows the SEM image of single powder particle forming corresponding small pores. (e) The SEM image of the pore on the HP-MG, the inset shows the SEM image of the nano powder particle forming corresponding mesopores. (f) The size distribution of pores on the HP-MG. (g) The TEM image of mesopores layer on the HP-MG. (h) The high-resolution TEM image of the single mesopore. (i) The element analysis of mesoporous layer on the HP-MG.

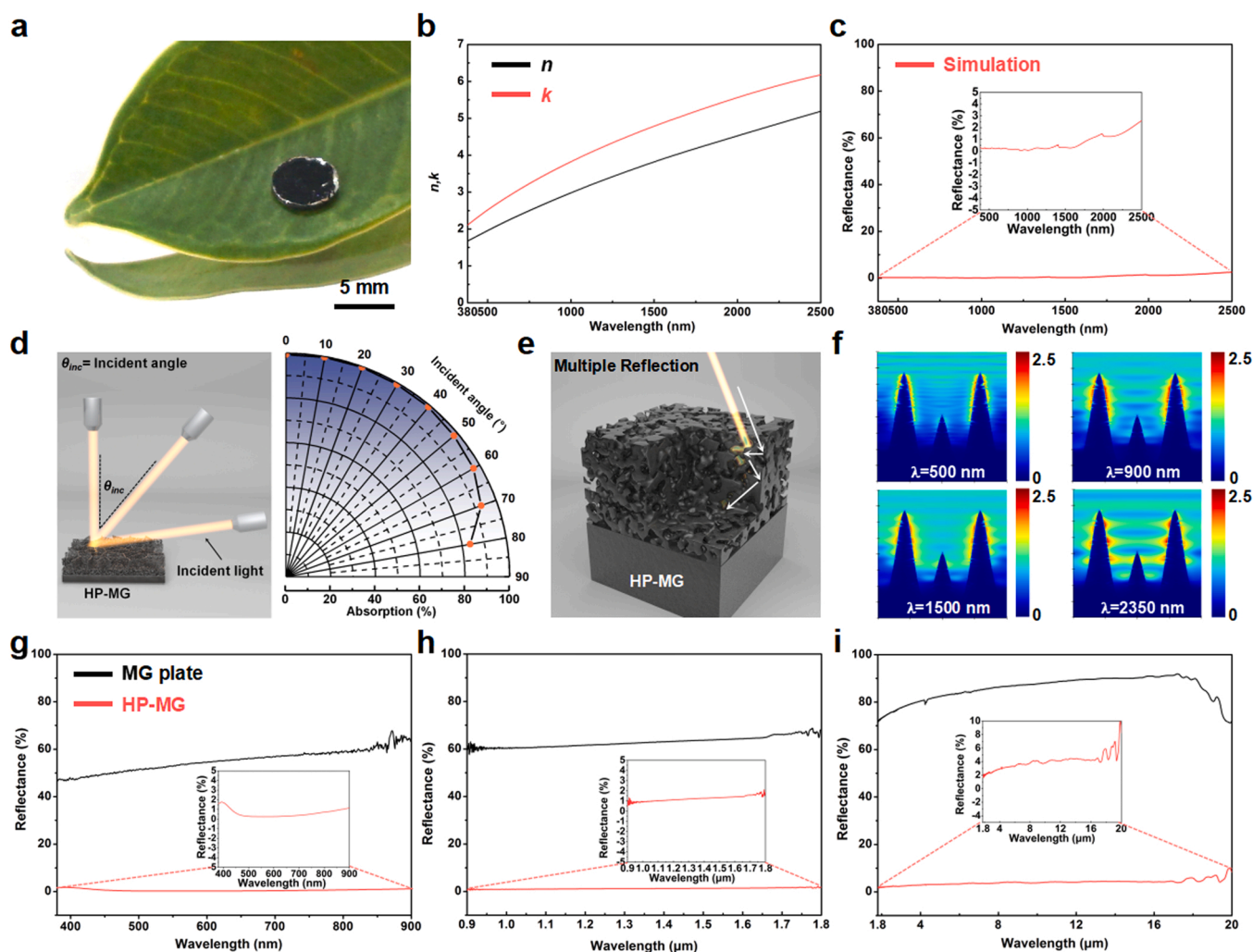


**Fig. 2.** The optical performance of HP-MG. (a) The photographic image of HP-MG. (b) The optical constants of MG plate. (c) The simulation reflectance spectrum of HP-MG from the 380–2500 nm at the normal incidence. (d) The schematic of different incident angles to HP-MG, and the simulated average absorption performance of HP-MG with the  $\theta_{inc}$ . (e) The multiple reflection enhancing the absorption of HP-MG. (f) The simulated cross section on electric field distributions of the HP-MG at the wavelengths of 500, 900, 1500, and 2350 nm. (g) The experimental reflectance spectrum of HP-MG and MG plate  $\lambda$  from 380 to 900 nm. (h) from 900 to 1800 nm. (i) from 1.8 to 20  $\mu\text{m}$ .

photothermal conversion performance setup. The HP-MG on the quartz was irradiated using five different wavelengths of laser (405, 532, 655, 808, and 1064 nm), and the temperature change was recorded by an IR camera during the irradiation. The high temperature stability of HP-MG was determined by irradiating the HP-MG with 808 nm laser with different powers. The test results can be found in the Fig. 3b. It can be seen that the laser power and the temperature rise showed a positive correlation. Notably, the temperature of the HP-MG can be increased to  $\sim 130^\circ\text{C}$  by 808 nm laser with power of  $6\text{ W/cm}^2$ , whereas the temperature of MG plate was only  $\sim 46^\circ\text{C}$  (Video S1 and Fig. S4). As it is mentioned above, the HP-MG shows a feature of the strong absorption in the broadband, it means that HP-MG can absorb light of different wavelengths. Subsequently, five different wavelengths of laser (405, 532, 655, 808, and 1064 nm) was applied to illuminate the HP-MG with energy power of  $0.5\text{ W/cm}^2$ . Fig. 3c-g record the temperature curve of HP-MG and MG plate, and the corresponding IR images are listed in Fig. 3i. Under the different wavelengths of laser light irradiation, the HP-MG can rapidly increase the surface temperature by  $\sim 7^\circ\text{C}$  within 5 s, and the temperature loss is not observed obviously after cyclic irradiation. In comparison, with the same power and laser irradiation, the temperature of MG plate is only increase  $\sim 1^\circ\text{C}$ . These results indicate that HP-MG has excellent photothermal conversion properties.

Meanwhile, its photothermal performance does not change after 9 cycles of irradiation when the HP-MG have been placed for a period of time, indicating the HP-MG have excellent stability at high temperature (Fig. S5). Fig. 3 h summarizes the heating rate of HP-MG and MG plate under the irradiation of different wavelength lasers and the 808 nm laser with different energy power. It can be seen that the heating rate is linearly dependent on the energy power from  $0.5$  to  $6\text{ W/cm}^2$ , and the maximum heating rate of  $32.25^\circ\text{C/s}$  is reached at  $6\text{ W/cm}^2$ . The heating rate of HP-MG is also significantly better than MG plate under irradiation of different wavelengths.

To demonstrate the superiority of our absorber, the previous work in the field of the light absorbers such as porous materials, nano materials, and films have been summarized in the Fig. 4a (Table S1). It can be seen that the broad absorption range ( $\sim 20\text{ }\mu\text{m}$ ) and the high heating rate ( $32.25^\circ\text{C/s}$ ) of HP-MG surpass the various absorbers reported to date (Fig. 4b). The maximum temperature ( $T_{max}$ ) of HP-MG under the irradiation can reach the  $\sim 130^\circ\text{C}$ , which is also slightly higher than many previously reported photothermal absorbers (Fig. 4c, d). The high temperature stability and photothermal performance at different wavelengths as well as excellent heating rate of HP-MG promise potential applications in field of photothermal switch, evaporation, catalysis, etc.

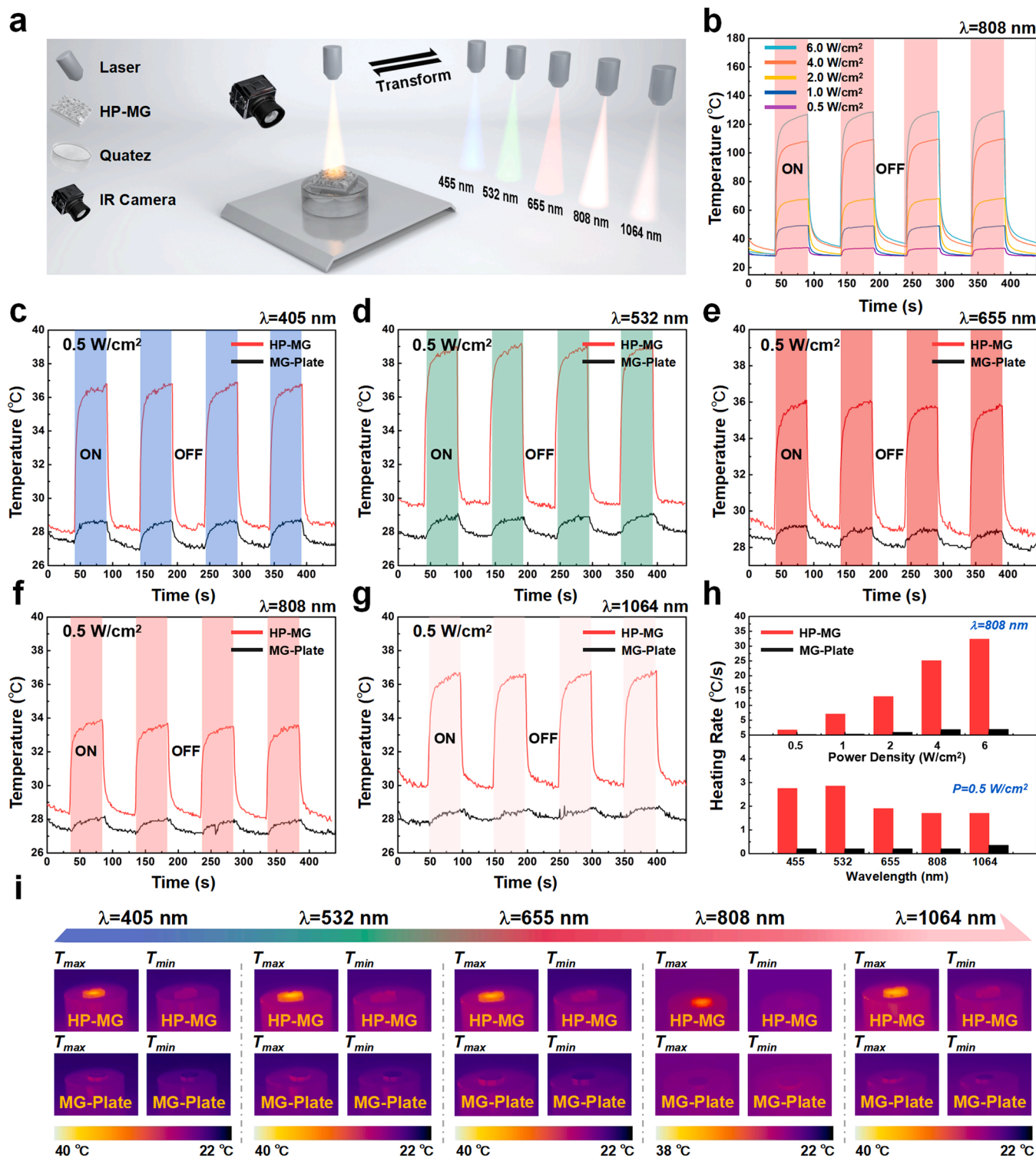


**Fig. 3.** The photothermal performance of HP-MG. (a) The schematic illustration of testing photothermal performance. (b) The temperature curve of the HP-MG irradiated with 808 nm laser with different energy power. (c) The temperature curve of the HP-MG and the MG plate irradiated with 405 nm laser with 0.5 W/cm<sup>2</sup>. (d) 532 nm. (e) 655 nm. (f) 808 nm. (g) 1064 nm. (h) The heating rate of the HP-MG and MG plate irradiated with 808 nm laser with different energy power, and the HP-MG and MG plate irradiated with different wavelength of 405, 532, 655, 808, and 1064 nm laser under 0.5 W/cm<sup>2</sup>. (i) The IR image of HP-MG and the MG plate irradiated with 405, 532, 655, 808, and 1064 nm laser under 0.5 W/cm<sup>2</sup>.

#### 2.4. The Evaporation Performance of the HP-MG

Inspired by the outstanding photothermal feature in the broadband and the HP structures of the HP-MG, the solar evaporation performance of the HP-MG is experimentally investigated. Fig. 5a shows the

schematic illustration of solar-driven water evaporation based on HP-MG. The details of experimental setup can be found in the Fig. S6. The foam with countersunk holes can carry the samples and absorb the water in the cuvette. When the foam carries the samples for measurement, the water in the foam will infiltrate the HP-MG surface from the

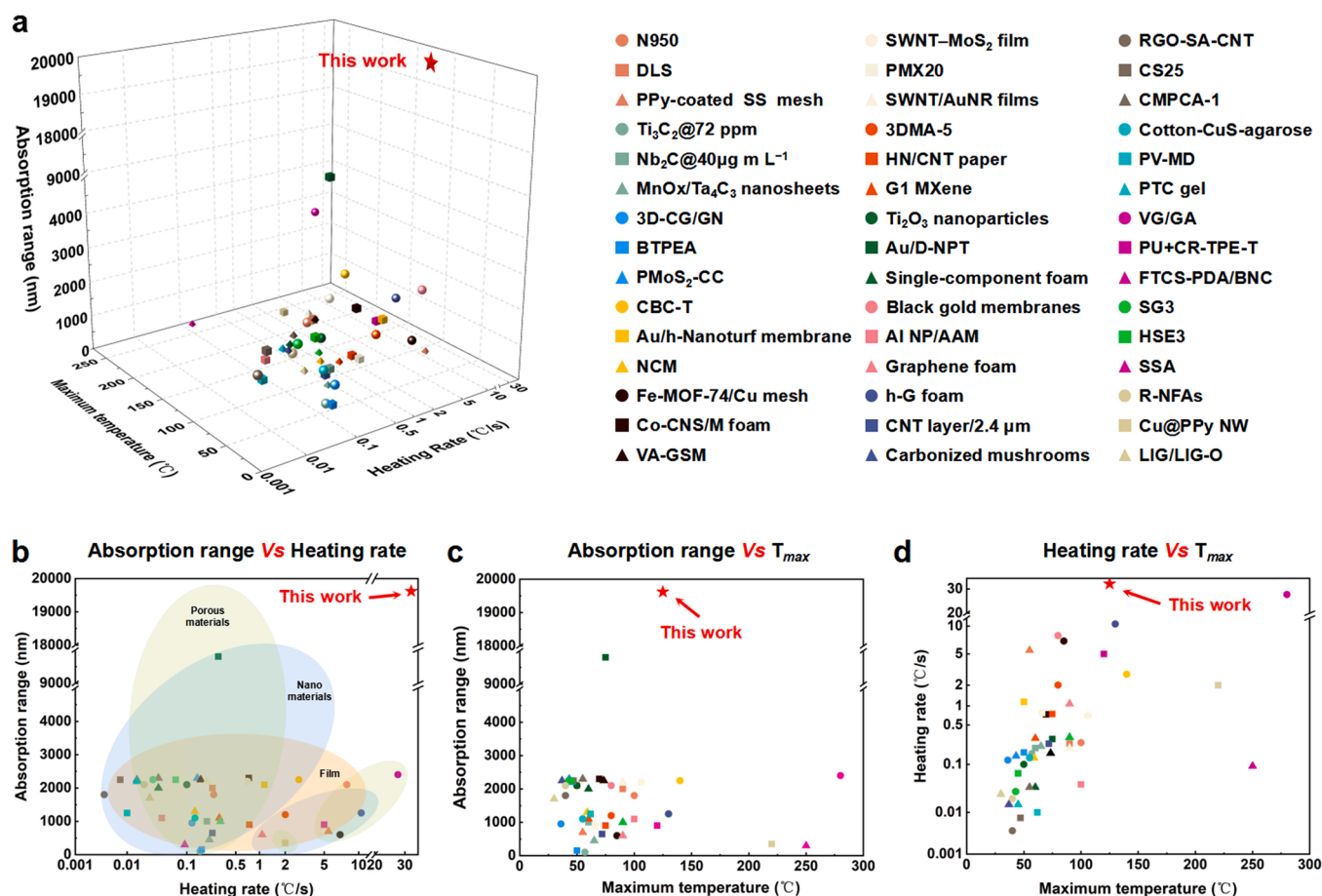


Fig. 4. The absorption range, heating rate  $T_{max}$  of HP-MG in the present work, compared with the previous photothermal materials. (a) The comparison of the absorption range,  $T_{max}$  and heating rate of the previous photothermal materials. (b) The detail comparison of the absorption range and heating rate of the previous absorber. (c) Absorption range vs  $T_{max}$ . (d) Heating rate vs  $T_{max}$ .

surroundings to achieve evaporation under the solar irradiation. Considering the water in the foam will also evaporate under solar irradiation, the bright tin foil will be used to wrap the cuvette so that only surface of the sample is exposed to the solar illumination. The ability of HP-MG to absorb light is a very important factor for solar steam generation. To quantify this performance, the UV-Vis-NIR absorption spectrum of HP-MG was measured. As can be seen, the HP-MG exhibits over 97% absorption over the solar spectrum (Fig. S7). Subsequently, the temperature change of HP-MG in the air and HP-MG + water was recorded under the  $1 \text{ kW m}^{-2}$  solar irradiation, and the corresponding temperature curve of the MG plate was also collected (Fig. 5b). It can be clearly seen that the temperature of HP-MG in the air and the HP-MG + water is remarkably higher than MG plate in the air and the MG plate + water. Respectively, HP-MG in the air and HP-MG + water will increase to the  $41.3$  and  $35.3$  °C over time. The IR images will more intuitively observe the temperature changes under the  $1 \text{ kW m}^{-2}$  solar irradiation from 0 to 900 s (Fig. 5c and Fig. S8). It is worth mentioning that the temperature of foam at the bottom will also increase at the same time during the HP-MG in the air was irradiated. When the foam area was covered with tin foil, the temperature only rises on the surface of the HP-MG, as shown in the IR images, indicating that the area covered with tin foil effectively reduces the evaporation in the foam area, which is more conducive to improve the measurement accuracy of the evaporation process. The speed of water infiltrating the sample surface from the foam can be reflected by the wettability. The change process before and after dripping a water droplet on the HP-MG and MG plate can be seen from the Fig. 5d (Video S2). The water droplet is immediately absorbed within 0.2 s after contacting the HP-MG surface. In contrast, the water

droplet contact angle on the MG plate changes from  $61^\circ$  to  $52^\circ$  within 16 s. This means that both HP-MG and MG plate exhibit hydrophilic behavior, but the HP-MG has a smaller water contact angle displaying the better hydrophilic property. It should be emphasized that the excellent wettability of HP-MG will rapidly supply water to enhance the efficient evaporation under the solar irradiation. Based on excellent hydrophilic and photothermal conversion performance, Fig. 5e quantitatively records the mass change of water for HP-MG, MG plate, and pure water under the  $1 \text{ kW m}^{-2}$  solar irradiation. It is obvious that HP-MG achieves the highest evaporation rate of  $1.72 \text{ kg m}^{-2} \text{ h}^{-1}$  compared to MG plate and pure water, which is 3.48 times that of pure water and 2.48 times that of MG plate. The evaporation efficiency of HP-MG is calculated by the following equations to be 94.2% (The detailed calculations are shown in Note S1).

$$\eta_{sv} = \frac{\dot{m}(H_{LV} + Q)}{E_{in}} \quad (1)$$

$$H_{LV} = 1.91846 * 10^6 * [T_{fin} / (T_{fin} - 33.91)]^2 \quad (2)$$

$$Q = c * (T_{fin} - T_{in}) \quad (3)$$

$\eta_{sv}$  is the evaporation conversion efficiency,  $\dot{m}$  is the evaporation rate under irradiation which has subtracted the evaporation rate under dark condition (Fig. S9),  $E_{in}$  represents the energy input of the incident light,  $H_{LV}$  shows the latent heat required for the vaporization of water,  $Q$  is the heat required for increasing the temperature of the water,  $c$  is the specific heat of the water,  $T_{fin}$  is the average temperature of the HP-MG surface during the evaporation, and  $T_{in}$  is the initial temperature of the

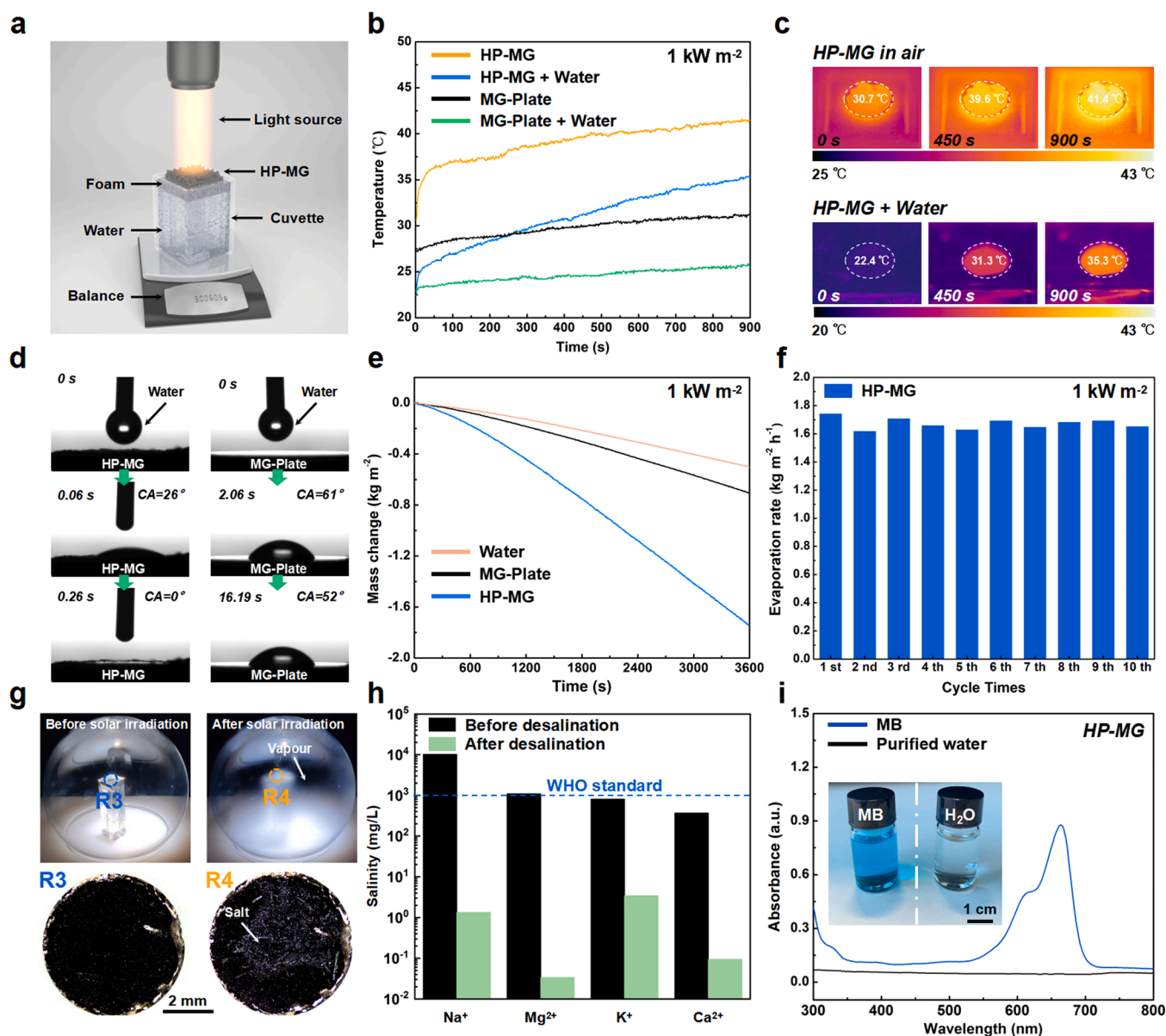


**Fig. 5.** The evaporation performance of the HP-MG. (a) The schematic illustration of solar-driven water evaporation for HP-MG. (b) The temperature curve of the HP-MG, HP-MG + water, MG plate and MG plate + water under 1 sun irradiation. (c) The IR images of the HP-MG and the HP-MG + water from 0 to 900 s under 1 sun irradiation. (d) The changes of contact angle of the HP-MG and the MG plate. (e) The mass change of the HP-MG, MG plate and water over time under 1 sun irradiation. (f) The reusability of the HP-MG under 1 solar irradiation. (g) The optical images of a glass cover and the change of HP-MG surface before, after solar irradiation for the water evaporation of HP-MG. (h) The measured concentrations of Na<sup>+</sup>, Mg<sup>2+</sup>, K<sup>+</sup>, Ca<sup>2+</sup> in an actual seawater sample (Huanghai Sea) before and after desalination, the dashed line represents the WHO standard. (i) The sewage treatment performance of HP-MG.

HP-MG surface [43,44].

Moreover, the reusability of HP-MG solar steam generation is examined to evaluate the possibility of practical application. The evaporation rate obtained by each irradiation is summarized in Fig. 5 f (Fig. S10), in which each evaporation rate of HP-MG did obvious no change after 10 cycles of solar irradiation. The good reusability of evaporation rate attribute to the self-supporting HP structure that is not easily destroyed on the MG. To demonstrate the desalination ability of HP-MG solar steam generation in seawater, the simulated seawater replaced the pure water. A glass cover was used to cover the HP-MG under the solar irradiation. After the solar irradiation whether indoors or outdoors, the steam evaporated from the HP-MG surface appeared on the glass wall, and some salt particles can be found on the surface of HP-MG (Fig. 5 g, Fig. S11, 12 and Video S3). The practical desalination ability of the HP-MG solar steam generation can be further assessed to

measure ion concentration of Na<sup>+</sup>, Mg<sup>2+</sup>, K<sup>+</sup>, Ca<sup>2+</sup> before and after desalination using the real seawater from Huanghai Sea, China (Fig. 5 h). The ion concentration in water collected by HP-MG solar steam generation under irradiation is nearly three orders of magnitude lower than the true seawater ion concentration, and meets the drink water standard set by the World Health Organization (WHO). The resistance value also verifies the ion concentration before and after desalination (Fig. S13). The sewage treatment ability of the HP-MG was evaluated using methylene blue as a pollutant. The MB solution was evaporated using the HP-MG evaporator, and the water obtained by evaporation is collected. Fig. 5i shows the UV-Vis-NIR absorbance spectra of the MB solution before and after the evaporation using the HP-MG evaporator. The MB have a strong absorption peak in the wavelength of 650 nm before evaporation, while the peak of the purified water collected after evaporation using the HP-MG evaporator is almost

completely eliminated. Meanwhile, the inset also can find the original blue solution became colourless. Indicating that the HP-MG solar steam generation has an efficient effect on sewage treatment. Finally, the stability of the HP-MG was also examined for evaporating seawater and MB. After each evaporation, water and ultrasonic cleaning will be used to rinse the HP-MG surface. The evaporation rates of seawater and MB from the HP-MG evaporator were initially measured at 1.53 and 1.62 kg m<sup>-2</sup> h, respectively (Fig. S14). After some cycles, the evaporation performance of the HP-MG for seawater and MB did not change significantly. These experimental results clearly display the potential of HP-MG solar steam generation for seawater desalination and sewage treatment applications.

### 3. Conclusion

In summary, we have successfully prepared HP structures on the MG in just 30 s. The HP-MG is an absorber with superb absorption properties. HP-MG can achieve more than 90% light absorption in the 380–20 μm wavelength range and the broad  $\theta_{inc}$  from 0° to 70°. The remarkable optical absorption effect is attributed to the capture of light by its surface porous structure, the multiple reflection of light in the HP structure and the induced LSPR on the surface of its disordered porous structure. Broadband and broad-angle light absorption performance enables the HP-MG absorber to exhibit excellent photothermal conversion performance. The HP-MG will rapidly reach 130 °C at a heating rate of 32.35 °C/s under the 808 nm laser power of 6 W/cm<sup>2</sup>. Additionally, the excellent hydrophilic properties of the HP-MG combined with the outstanding photothermal performance, allow it to be used directly for efficient solar steam generation. The solar steam generator shows a very rapid evaporation rate of 1.72 kg m<sup>-2</sup> h<sup>-1</sup> and a solar evaporation efficiency of up to 94.2% under one solar irradiation. Meanwhile, we have confirmed its practicality for seawater desalination and wastewater treatment. We believe that the HP-MG absorber will have an influence on many potential fields of application, such as photocatalysis, photodetectors, photothermal imaging, etc.

## 4. Experimental section

### 4.1. Materials

The MG system (Pt<sub>57.5</sub>Ni<sub>14.7</sub>Cu<sub>5.3</sub>P<sub>22.5</sub>) was selected chosen for the experiment due to the Pt-based MG has wide SLR and excellent TPF ability (Fig. S15) [45]. The high purity (>99.95 at%) raw metallic materials Pt, Ni and Cu were arc-melted in argon atmosphere to form master alloy ingot. Then the master alloy ingot and high purity P (>99.999 at%) were sealed in quartz tubes for induction melting in argon atmosphere to obtain the alloy ingot with nominal composition of Pt<sub>57.5</sub>Ni<sub>14.7</sub>Cu<sub>5.3</sub>P<sub>22.5</sub>.

The cylindrical rods of Pt<sub>57.5</sub>Ni<sub>14.7</sub>Cu<sub>5.3</sub>P<sub>22.5</sub> MG with the diameter of 5 mm were fabricated by the same method of copper-mold casting in an argon atmosphere.

The BaTiO<sub>3</sub> powder with an average particle size of ~ 40 nm was purchased by Zhongke Yannuo New Material Technology Co., Ltd in Beijing.

### 4.2. The Detail of TPF

The prepared Pt-based MG cylindrical rods were cut into circular plates with a thickness of ~ 1 mm. The plates were polished on both sides to ensure that the Pt-based MG surface can better form HP structures by TPF. The polished Pt-based MG surface was covered by BaTiO<sub>3</sub> powder and then sent to the heated chamber with a vacuum of 6 × 10<sup>-3</sup> Pa. When the temperature rises to 538 K, the pressure of 421 MPa was applied to the surface of Pt-based MG, and the pressure was maintained until the surface temperature reaches 548 K, this process can be completed within 30 s. Then the sample was taken out of the heating

chamber, the sample after cooling will be immersed in 3 mol HCl for two hours to remove the BaTiO<sub>3</sub> powder on the Pt-based MG.

### 4.3. The Multiscale Characterization

X-ray diffraction (XRD; Rigaku MiniFlex 600) with Cu K $\alpha$  radiation was used to detect the amorphous properties of origin Pt-based MG and the MG surface of hierarchical structures (HP-MG). Differential scanning calorimetry (DSC; Perkin-Elmer DSC-8000) with a cooling/heating rate of 20 K/min was used to ascertain the glass transition temperature ( $T_g$ ), crystallization temperature ( $T_c$ ) of origin Pt-based MG and SLR. Scanning electron microscope (SEM; Fei quanta FEG 450) was recorded by the morphology of hierarchical structures. The atomic structure and the meticulous morphology of hierarchical structures was characterized in a JEM-2100 F TEM with energy disperse spectroscopy (EDS).

### 4.4. The FDTD Simulation

The FDTD we used is based on Maxwell's equations, which can be used to calculate the reflectance. We set the periods of randomly distributed nanostructures as 2 μm × 2 μm, 4 μm × 4 μm, 8 μm × 8 μm and 16 μm × 16 μm, respectively, to calculate their reflectance, and the calculated results have no obvious change (Fig. S16). To simplify the model, the region of 2 μm × 2 μm was used for later simulated calculation. Furthermore, to better fit the hierarchical porous structure of the experiment, the mesoporous layer is constructed by using air holes with a particle size of ~ 60 nm in the region of 2 μm × 2 μm (Fig. S17). In the calculation process, periodic boundary conditions are used in the X and Y directions, and perfect matching layer conditions are used in the Z direction. 2 nm × 2 nm × 2 nm grid division method is adopted to ensure the correctness of simulation results. The light source is excited by a plane wave.

### 4.5. The Optical Characterization

The reflection spectrum (from 380 to 800 nm) of Pt-based MG and HP-MG was tested by a microspectral measurement system (Hangzhou SPL; ProSp-Micro40-VIS). Fourier transform infrared spectrometer (Vertex 70; Bruker) with an integrating sphere was used to measure the reflectance of sample in the near-infrared and mid-infrared wavelength regions. The optical constants of Pt-based MG were measured by ellipsometer (J.A Woollam RC2-XI) from 380 nm to 2500 nm.

### 4.6. The Photothermal Characterization

The laser of 405 nm (PGL-V-H-405), 532 nm (PGL-V-H-532), 655 nm (PGL-V-H-655), 808 nm (5 W, fiber-tailed, multimode diode laser), 1064 nm (PGL-V-H-1064) were used to characterize the photothermal effect of the Pt-based MG and HP-MG. The sample was placed on a quartz and the laser switch cycle was 100 s, and then laser irradiated the sample vertically to 450 s. The infrared imaging camera (Fotric 280d) was used to monitor the thermal response of the surface during this process with a data acquisition frequency of 1 Hz.

### 4.7. Water Evaporation Characterization

A Xe light (CEL-HXF 300, Beijing Education Au-light Co., Ltd.) with an AM 1.5 filter was set at the top of the samples to simulate as the sunlight. The light intensity was monitored by a strong light power meter (CEL-NP2000, Beijing Education Au-light Co., Ltd.). The temperature was measured using an infrared thermal imager (Fotric 280d). The contact angle of the samples was measured using a droplet shape analyzer (DSA100S, Krüss, Germany), the volume of water droplets was 1 μL. The mass of evaporation loss of samples was measured with an electronic balance (Sartorius Quintix35-1CN, measurement accuracy 0.01 mg) connected with the computer. The concentration of Na<sup>+</sup>, K<sup>+</sup>,

Ca<sup>2+</sup>, and Mg<sup>2+</sup> were collected by atomic emission spectrometry with inductively coupled plasma (ICPA 7400). The absorbance spectrum (from 300 to 800 nm) was measured a UV-Vis-NIR spectrophotometer (Shimadzu UV-1280).

The 3.37 g of NaCl, 1.63 g of MgSO<sub>4</sub>, 1.13 g of MgCl<sub>2</sub>, 0.58 g of CaCl<sub>2</sub> and 0.36 g of KCl were added into 500 mL of deionized water and dissolved completely to get simulated seawater.

### CRedit authorship contribution statement

**Jianan Fu:** Methodology, Data curation, Writing – original draft, Investigation, Formal analysis. **Zhen Li:** Writing – review & editing, Formal analysis, Methodology, Data curation. **Xin Li:** Methodology, Formal analysis. **Fei Sun:** Visualization, Validation. **Luyao Li:** Formal analysis, Data curation. **Hongzhen Li:** Formal analysis, Validation. **Jinlai Zhao:** Validation, Formal analysis, Resources. **Jiang Ma:** Conceptualization, Validation, Writing – review & editing, Project administration, Funding acquisition, Supervision.

### Declaration of Competing Interest

The authors declare that they have no known competing financial interests or personal relationships that could have appeared to influence the work reported in this paper.

### Data Availability

Data will be made available on request.

### Acknowledgements

The work was supported by the Key Basic and Applied Research Program of Guangdong Province, China (Grant Nr. 2019B030302010), the NSF of China (Grant No. 52122105, 51871157, 51971150), the National Key Research and Development Program of China (Grant No. 2018YFA0703605), the National Natural Science Foundation of China (No. 62105220), Guangdong Provincial Basic and Applied Basic Research Fund Regional Joint Fund Project (No. 2020A1515110750). The authors also thank the assistance on microscope observation received from the Electron Microscope Center of the Shenzhen University.

### Appendix A. Supporting information

Supplementary data associated with this article can be found in the online version at [doi:10.1016/j.nanoen.2022.108019](https://doi.org/10.1016/j.nanoen.2022.108019).

### References

- [1] N.S. Lewis, Toward cost-effective solar energy use, *science* 315 (2007) 798–801.
- [2] Y. Wang, L. Zhang, P. Wang, Self-floating carbon nanotube membrane on macroporous silica substrate for highly efficient solar-driven interfacial water evaporation, *ACS Sustain. Chem. Eng.* 4 (2016) 1223–1230.
- [3] N. Li, X. Niu, L. Li, H. Wang, Z. Huang, Y. Zhang, Y. Chen, X. Zhang, C. Zhu, H. Zai, Liquid medium annealing for fabricating durable perovskite solar cells with improved reproducibility, *Science* 373 (2021) 561–567.
- [4] H. Min, D.Y. Lee, J. Kim, G. Kim, K.S. Lee, J. Kim, M.J. Paik, Y.K. Kim, K.S. Kim, M. G. Kim, Perovskite solar cells with atomically coherent interlayers on SnO<sub>2</sub> electrodes, *Nature* 598 (2021) 444–450.
- [5] A. Aubele, Y. He, T. Kraus, N. Li, E. Mena-Osteritz, P. Weitz, T. Heumüller, K. Zhang, C.J. Brabec, P. Bäuerle, Molecular oligothiophene–fullerene dyad reaching over 5% efficiency in single-material organic solar cells, *Adv. Mater.* (2021) 2103573.
- [6] S. Tian, Z. Huang, J. Tan, X. Cui, Y. Xiao, Y. Wan, X. Li, Q. Zhao, S. Li, C.-S. Lee, Manipulating interfacial charge-transfer absorption of cocrystal absorber for efficient solar seawater desalination and water purification, *ACS Energy Lett.* 5 (2020) 2698–2705.
- [7] Z. Liu, Z. Zhou, N. Wu, R. Zhang, B. Zhu, H. Jin, Y. Zhang, M. Zhu, Z. Chen, Hierarchical photothermal fabrics with low evaporation enthalpy as heliotropic evaporators for efficient, continuous, salt-free desalination, *ACS Nano* 15 (2021) 13007–13018.
- [8] H. Yao, P. Zhang, C. Yang, Q. Liao, X. Hao, Y. Huang, M. Zhang, X. Wang, T. Lin, H. Cheng, Janus-interface engineering boosting solar steam towards high-efficiency water collection, *Energy Environ. Sci.* 14 (2021) 5330–5338.
- [9] H. Niu, J. Li, X. Wang, F. Luo, Z. Qiang, J. Ren, Solar-Assisted, Fast, and In Situ Recovery of Crude Oil Spill by a Superhydrophobic and Photothermal Sponge, *ACS Appl. Mater. Interfaces* 13 (2021) 21175–21185.
- [10] M.B. Wu, S. Huang, T.Y. Liu, J. Wu, S. Agarwal, A. Greiner, Z.K. Xu, Compressible carbon sponges from delignified wood for fast cleanup and enhanced recovery of crude oil spills by joule heat and photothermal effect, *Adv. Funct. Mater.* 31 (2021) 2006806.
- [11] X. Ma, C. Zhang, P. Gnanasekar, P. Xiao, Q. Luo, S. Li, D. Qin, T. Chen, J. Chen, J. Zhu, Mechanically robust, solar-driven, and degradable lignin-based polyurethane adsorbent for efficient crude oil spill remediation, *Chem. Eng. J.* 415 (2021), 128956.
- [12] A.M. Saleque, S. Ahmed, M.N.A.S. Ivan, M.I. Hossain, W. Qarony, P.K. Cheng, J. Qiao, Z.L. Guo, L. Zeng, Y.H. Tsang, High-temperature solar steam generation by MWCNT-HfTe<sub>2</sub> van der Waals heterostructure for low-cost sterilization, *Nano Energy* 94 (2022), 106916.
- [13] L. Zhao, B. Bhatia, L. Zhang, E. Strobach, A. Leroy, M.K. Yadav, S. Yang, T. A. Cooper, L.A. Weinstein, A. Modi, A passive high-temperature high-pressure solar steam generator for medical sterilization, *Joule* 4 (2020) 2733–2745.
- [14] P. Tao, G. Ni, C. Song, W. Shang, J. Wu, J. Zhu, G. Chen, T. Deng, Solar-driven interfacial evaporation, *Nat. Energy* 3 (2018) 1031–1041.
- [15] C. Chen, Y. Kuang, L. Hu, Challenges and opportunities for solar evaporation, *Joule* 3 (2019) 683–718.
- [16] A.M. Saleque, S. Ma, S. Ahmed, M.I. Hossain, W. Qarony, Y.H. Tsang, Solar driven interfacial steam generation derived from biodegradable luffa sponge, *Adv. Sustain. Syst.* 5 (2021) 2000291.
- [17] A.M. Saleque, N. Nowshin, M.N.A.S. Ivan, S. Ahmed, Y.H. Tsang, Natural porous materials for interfacial solar steam generation toward clean water production, *Sol. RRL* 6 (2022) 2100986.
- [18] J. He, Z. Zhang, C. Xiao, F. Liu, H. Sun, Z. Zhu, W. Liang, A. Li, High-performance salt-rejecting and cost-effective superhydrophilic porous monolithic polymer foam for solar steam generation, *ACS Appl. Mater. Interfaces* 12 (2020) 16308–16318.
- [19] X. Dong, Y. Si, C. Chen, B. Ding, H. Deng, Reed leaves inspired silica nanofibrous aerogels with parallel-arranged vessels for salt-resistant solar desalination, *ACS Nano* (2021).
- [20] H. Ren, M. Tang, B. Guan, K. Wang, J. Yang, F. Wang, M. Wang, J. Shan, Z. Chen, D. Wei, Hierarchical graphene foam for efficient omnidirectional solar–thermal energy conversion, *Adv. Mater.* 29 (2017) 1702590.
- [21] X. Fan, Y. Yang, X. Shi, Y. Liu, H. Li, J. Liang, Y. Chen, A MXene-based hierarchical design enabling highly efficient and stable solar-water desalination with good salt resistance, *Adv. Funct. Mater.* 30 (2020) 2007110.
- [22] W.-H. Wang, C. Dong, C. Shek, Bulk metallic glasses, *Mater. Sci. Eng., R.* 44 (2004) 45–89.
- [23] J. Schroers, Processing of bulk metallic glass, *Adv. Mater.* 22 (2010) 1566–1597.
- [24] A. Inoue, A. Takeuchi, Recent development and application products of bulk glassy alloys, *Acta Mater.* 59 (2011) 2243–2267.
- [25] J. Ma, C. Yang, X. Liu, B. Shang, Q. He, F. Li, T. Wang, D. Wei, X. Liang, X. Wu, Fast surface dynamics enabled cold joining of metallic glasses, *Sci. Adv.* 5 (2019) eaax7256.
- [26] Z. Li, J. Ma, Water-repellent surfaces of metallic glasses: fabrication and application, *Mater. Today Adv.* 12 (2021), 100164.
- [27] J. Fu, J. Yang, K. Wu, H. Lin, W. Wen, W. Ruan, S. Ren, Z. Zhang, X. Liang, J. Ma, Metallic Glue for Designing Composite Materials with Tailorable Properties, *Mater. Horiz.* (2021).
- [28] H. Li, Z. Li, J. Yang, H.B. Ke, B. Sun, C.C. Yuan, J. Ma, J. Shen, W.H. Wang, Interface design enabled manufacture of giant metallic glasses, *Sci. China Mater.* 64 (2021) 964–972.
- [29] X. Li, D. Wei, J. Zhang, X. Liu, Z. Li, T. Wang, Q. He, Y. Wang, J. Ma, W. Wang, Ultrasonic plasticity of metallic glass near room temperature, *Applied, Mater. Today* 21 (2020), 100866.
- [30] J. Fu, Z. Huang, J. Yang, J. Ma, J. Shen, Nano-forming of the rare earth La-based metallic glass, *J. Non-Cryst. Solids* 558 (2021), 120682.
- [31] Y. Yan, C. Wang, Z. Huang, J. Fu, Z. Lin, X. Zhang, J. Ma, J. Shen, Highly efficient and robust catalysts for the hydrogen evolution reaction by surface nano engineering of metallic glass, *J. Mater. Chem. A* (2021).
- [32] A. Aditya, H.F. Wu, H. Arora, S. Mukherjee, Amorphous metallic alloys: pathways for enhanced wear and corrosion resistance, *JOM* 69 (2017) 2150–2155.
- [33] J. Ma, X. Zhang, D. Wang, D. Zhao, D. Ding, K. Liu, W. Wang, Superhydrophobic metallic glass surface with superior mechanical stability and corrosion resistance, *Appl. Phys. Lett.* 104 (2014), 173701.
- [34] C. Uzun, C. Meduri, N. Kahler, L.G. De Peralta, J.M. McCollum, M. Pantoya, G. Kumar, A.A. Bernussi, Photoinduced heat conversion enhancement of metallic glass nanowire arrays, *J. Appl. Phys.* 125 (2019), 015102.
- [35] C. Uzun, N. Kahler, L. Grave de Peralta, G. Kumar, A.A. Bernussi, Photo-induced-heat localization on nanostructured metallic glasses, *J. Appl. Phys.* 122 (2017), 094306.
- [36] P. Mu, Z. Zhang, W. Bai, J. He, H. Sun, Z. Zhu, W. Liang, A. Li, Superwetting monolithic hollow-carbon-nanotubes aerogels with hierarchically nanoporous structure for efficient solar steam generation, *Adv. Energy Mater.* 9 (2019) 1802158.
- [37] H.-J. Qiu, J. Wang, P. Liu, Y. Wang, M. Chen, Hierarchical nanoporous metal/metal-oxide composite by dealloying metallic glass for high-performance energy storage, *Corros. Sci.* 96 (2015) 196–202.

- [38] M. Meng, R. Li, L. Zuo, X. Luo, T. Zhang, Fabrication of hierarchical porous metallic glasses decorated with Cu nanoparticles as integrated electrodes for high-performance non-enzymatic glucose sensing, *Scr. Mater.* 199 (2021), 113884.
- [39] Z. Lu, Y. Yin, Colloidal nanoparticle clusters: functional materials by design, *Chem. Soc. Rev.* 41 (2012) 6874–6887.
- [40] Y. Tian, X. Liu, A. Caratenuto, J. Li, S. Zhou, R. Ran, F. Chen, Z. Wang, K.-T. Wan, G. Xiao, A new strategy towards spectral selectivity: Selective leaching alloy to achieve selective plasmonic solar absorption and infrared suppression, *Nano Energy* 92 (2022), 106717.
- [41] W. Sun, A. Du, Y. Feng, J. Shen, S. Huang, J. Tang, B. Zhou, Super black material from low-density carbon aerogels with subwavelength structures, *ACS Nano* 10 (2016) 9123–9128.
- [42] J.B. Chou, Y.X. Yeng, Y.E. Lee, A. Lenert, V. Rinnerbauer, I. Celanovic, M. Soljačić, N.X. Fang, E.N. Wang, S.G. Kim, Enabling ideal selective solar absorption with 2D metallic dielectric photonic crystals, *Adv. Mater.* 26 (2014) 8041–8045.
- [43] M.N.A. Ivan, A.M. Saleque, S. Ahmed, P.K. Cheng, J.P. Qiao, T.I. Alam, Y.H. Tsang, Waste egg tray and toner-derived highly efficient 3D solar evaporator for freshwater generation, *ACS Appl. Mater. Interfaces* 14 (2022) 7936–7948.
- [44] X. Wu, M.E. Robson, J.L. Phelps, J.S. Tan, B. Shao, G. Owens, H.L. Xu, A flexible photothermal cotton-CuS nanocage-agarose aerogel towards portable solar steam generation, *Nano Energy* 56 (2019) 708–715.
- [45] G. Kumar, H.X. Tang, J. Schroers, Nanomoulding with amorphous metals, *Nature* 457 (2009) 868–872.



**Fei Sun** received his BSc degree in mechanical engineering from Wuhan Institute of Technology in 2015 and the MA degree from Shenzhen University, Shenzhen, China, in 2019. His research includes metallic glasses, composite materials. His research includes metallic glasses, composite materials, and micro/nano-forming of glass.



**Luyao Li** is currently a MA student at the College of Mechatronics and Control Engineering, Shenzhen University. His research interests include metallic glass, high-entropy alloys, and advanced manufacturing.



**Hongzhen Li** received his master degree in mechanical engineering from Shenzhen University in 2020. Currently, he is studying for a PhD at South China University of Technology. His research includes metallic glass, high-entropy alloys, and advanced manufacturing.



**Jinlai Zhao** is currently an associate researcher in College of Materials Science and Engineering, Shenzhen University. He received master degree in materials engineering from Shenzhen University in 2013. He received Ph.D. degree from Macao University Science and Technology (MUST) in 2020. He was awarded Macao Special Administrative Region Postgraduate Research and Development in 2020. He is now a Shenzhen Peacock Overseas high-level talent Class C. He has published about 40 SCI peer-reviewed journal papers with about 2700 citations, H-index is 25. His research focuses on the anisotropic photodetectors and stress control of two-dimensional materials (MoS<sub>2</sub>, Black phosphorus etc.), the mechanical performance for soft materials by atomic force microscope (AFM).



**Jiang Ma** received his BSc degree in materials science and engineering from Southeast University in 2009 and PhD degree from the Institute of Physics, Chinese Academy of Sciences (CAS), in 2014. He is currently a Professor at the College of Mechatronics and Control Engineering, Shenzhen University. His research includes metallic glass, high-entropy alloy, micro/nano precision forming, and functional surface fabrication and application.



**Jianan Fu** entered Shenzhen University to study for a MA degree in 2019. His tutor is Jiang Ma, a professor of Shenzhen University. He is studying for a Ph.D. in the Southern University of Science and Technology (SUSTech). His research includes micro/nano-forming and functional application of metallic glass.



**Zhen Li** received the Ph.D. degree from Beihang University (BUAA), Beijing, China, in 2019, and he is currently working in Southern University of Science and Technology (SUSTech), Shenzhen, China. His research includes high entropy alloy, metallic glasses, composite material, advanced manufacturing, and surface engineering.



**Xin Li** received his BSc degree in mechanical engineering from East China University of Technology in 2018 and the MA degree from Shenzhen University, Shenzhen, China, in 2021. He is studying for a Ph.D. in the school of Mechanical, Electrical & Information Engineering, Shandong University, Weihai. His research includes metallic glasses, ultrasonic machining of metallic glass and so on.